

Rapidly growing primordial black holes as seeds of the massive high-redshift JWST GalaxiesGUAN-WEN YUAN ^{1,2,3} LEI LEI ^{1,2} YUAN-ZHU WANG ¹ BO WANG ^{2,4} YI-YING WANG ^{1,2} CHAO CHEN ⁵
ZHAO-QIANG SHEN ¹ YI-FU CAI ^{2,4} AND YI-ZHONG FAN ^{1,2}¹Key Laboratory of Dark Matter and Space Astronomy, Purple Mountain Observatory, Chinese Academy of Sciences, Nanjing 210023, People's Republic of China²School of Astronomy and Space Science, University of Science and Technology of China, Hefei 230026, People's Republic of China³Theoretical Physics Division, Institute of High Energy Physics, Chinese Academy of Sciences, Beijing 100049, China⁴Deep Space Exploration Laboratory/Department of Astronomy, School of Physical Sciences, University of Science and Technology of China, Hefei 230026, People's Republic of China⁵Jockey Club Institute for Advanced Study, The Hong Kong University of Science and Technology, Hong Kong, China**ABSTRACT**

A group of massive galaxies at redshifts of $z \gtrsim 7$ have been recently detected by the James Webb Space Telescope (JWST), which were unexpected to form at such early time within the standard Big Bang cosmology. In this work, we propose that this puzzle can be explained by the presence of some primordial black holes (PBHs) with mass of $\sim 1000M_{\odot}$. These PBHs act as seeds for early galaxies formation with masses of $\sim 10^8 - 10^{10} M_{\odot}$ at high redshift, hence accounting for the JWST observations. We use a hierarchical Bayesian inference framework to constrain the PBH mass distribution models, and find that the Lognormal model with the $M_c \sim 750M_{\odot}$ is preferred over other hypotheses. These rapidly growing BHs are expected to have strong radiation and may appear as the high-redshift compact objects, similar to those recently discovered by JWST.

1. INTRODUCTION

The standard Big Bang cosmology, which has been supported by numerous precise cosmological measurements, has achieved remarkable success. However, in the past decade, observations and measurements have challenged some of its predictions (Perivolaropoulos & Skara 2022). Especially, the possibility that primordial black holes (PBHs) could be responsible for some observed phenomena has garnered considerable attention recently, in part because they could serve as both dark matter candidates and the seeds of supermassive black holes (SMBH) in high-redshift galaxies (Green & Kavanagh 2021; Inayoshi et al. 2020). Therefore, investigating PBHs presents an exciting opportunity to explore the mechanics of the early Universe (Escrivà et al. 2022).

PBHs, with far-reaching cosmological implications, can be formed through the gravitational collapse of overdense regions in the early Universe (Zel'dovich & Novikov 1966; Hawking 1971). These kinds of objects may have diverse masses and then account for various cosmological phenomena. Specifically, asteroid-mass PBHs can be applied to account for a sig-

nificant fraction of dark matter (Montero-Camacho et al. 2019), while PBHs with masses of hundreds $M \sim \mathcal{O}(10)M_{\odot}$ are viewed as candidate sources for LIGO/Virgo events (Bird et al. 2016; Sasaki et al. 2016). Moreover, PBHs with masses $M \sim \mathcal{O}(10^3)M_{\odot}$ are thought to be hypothetical seeds for high-redshift supermassive black holes (SMBHs), which is the focus of this work.

The upcoming JWST observations are expected to shed further light on the nature of high-redshift galaxies and the role of PBHs in their formation, whose formation mechanisms remain unclear (Gardner et al. 2006; Volonteri et al. 2021). Recently, its observations have identified several bright galaxy candidates at $z \gtrsim 7$ (Labbe et al. 2022; Atek et al. 2023; Yan et al. 2023), which are difficult to reconcile with the Big Bang cosmology predictions (Volonteri et al. 2021; Lovell et al. 2023). One possible interpretation is the alteration of the matter power spectrum by the PBHs (Liu & Bromm 2022; Biagetti et al. 2023; Trinca et al. 2023; Hütsi et al. 2023; Cai et al. 2023). In this work, we show that PBHs with masses of $\sim 1000M_{\odot}$ could potentially grow up into SMBHs with masses of $10^4 - 10^8 M_{\odot}$ observed in the centers of galaxies, through super-Eddington accretion within the dark matter halo. Then, we adopt a

¹ zqshen@pmo.ac.cn; yifucai@ustc.edu.cn; yzfan@pmo.ac.cn

hierarchical Bayesian inference framework to constrain the PBH mass distribution models, and find that the Lognormal model with the $M_c \sim 650M_\odot$ is strongly preferred over other hypotheses. These growing PBHs with strong radiation may appear as high-redshift compact objects, which accounted for those observations of JWST.

2. PBH EVOLUTION IN THE EARLY UNIVERSE

After having been generated, PBHs may evolve through accretion throughout cosmic history, and this accretion of baryonic matter onto PBHs can significantly impact their masses (De Luca et al. 2020a; Serpico et al. 2020). However, the physics of accretion is complex, as the accretion rate and the geometry of the accretion flow are intertwined and both play a crucial role in the evolution of the PBH masses. An analytic accretion model, such as the one developed by Mack, Ricotti and Ostriker (Mack et al. 2007; Ricotti 2007; Ricotti et al. 2008), can be used to study the accretion of baryonic matter onto PBHs and provide useful insights into the accretion behavior. In the intergalactic medium, a PBH with mass M can accrete baryonic matter at the Bondi-Hoyle rate \dot{M}_B which can be expressed as

$$\dot{M}_B = 4\pi\lambda m_H n_{\text{gas}} v_{\text{eff}}^2 r_B^2, \quad (1)$$

where $r_B = GM/v_{\text{eff}}^2$ is the Bondi-Hoyle radius, n_{gas} is the hydrogen gas number density, and $v_{\text{eff}} = \sqrt{v_{\text{rel}}^2 + c_s^2}$ is the PBH effective velocity, which is defined in terms of the PBH relative velocity v_{rel} and the gas with sound speed c_s . The accretion parameter λ accounts for the gas viscosity, the Hubble expansion, and the Compton scattering between the gas and the CMB, which is defined in Eq.(23) in Ricotti et al. (2008).

It is important to note that PBHs only make up a tiny portion of DM in the Universe, and that there is a dominant dark matter halo surrounding a PBH and expands over time as long as the PBHs do not interact with one another. This dark matter halo, or "dark matter clothing", increases the gas accretion rate, acting as a catalyst for PBH accretion despite the fact that the direct DM accretion is negligible for the PBH evolution. We assume that a black hole is surrounded by a dark halo with a density profile of $\rho \sim r^{-2.25}$ (Bertschinger 1985) and a characteristic radius of r_h . As long as the Bondi radius r_B is greater than twice the radius of the dark halo r_h , the gas accretion rate onto the halo is the same as that onto a bare PBH with a dark halo mass M_h . However, for that with smaller r_B or larger r_h , the accretion enhancement caused by the halo will take place and the accretion parameter must be modified to introduce corrections to the naked case following the

method in Ricotti et al. (2008) and Ricotti (2007). For instance, a thin accretion disk arises around the PBH if the angular momentum carried by the baryonic infalling material is sufficiently high.

The gas accretion rate is suppressed by the outflows from the PBH which sweep away the surrounded medium and only leave the diluted and hot gas. The integration of this effect, known as mechanical feedback (MF), into the analytic accretion calculation poses significant challenges (Ali-Haïmoud & Kamionkowski 2017; De Luca et al. 2020b). However, a glimmer of optimism arises from recent 3D numerical simulations (Bosch-Ramon & Bellomo 2020; Bosch-Ramon 2022; Piga et al. 2022). These simulations have provided valuable insights, suggesting a roughly consistent fractional rescaling factor for PBH accretion. As a result, we can succinctly express PBH accretion as $\dot{M}_{\text{acc}} = f_{\text{MF}} \dot{M}_B$, with an adopted value of $f_{\text{MF}} \simeq 0.15$. This selection is derived from averaging the potential outflow orientation angles during the accretion process. While this reduction in the accretion rate is significant, it serves as an illustrative example of PBH evolution in the early universe. A comprehensive analysis of these additional phenomena is a subject for future investigation, expanding our understanding of this intricate process.

After considering the effect of the dark halo and the feedback, the efficiency and shape of the accretion process are entirely encoded in the dimensionless baryonic accretion rate \dot{m} , which is defined as $\dot{m} = \dot{M}_{\text{acc}}/\dot{M}_{\text{Edd}}$ with the Eddington accretion $\dot{M}_{\text{Edd}} = 1.44 \times 10^{17} (M/M_\odot) \text{ g s}^{-1}$.

In Figure 1, we present the accretion rate \dot{m} as a function of PBH mass and redshift, leveraging data sources listed in Table 1 through the relationship between M_\star and M_{BH} . The black dotted lines illustrate the trajectories of PBH evolution for various initial masses, including $20M_\odot$, $40M_\odot$, $80M_\odot$, $160M_\odot$, $320M_\odot$, $640M_\odot$, $1280M_\odot$ and $2560M_\odot$ within the (M, z) plane. It is worth noting that the redshift cutoff for PBH accretion is set at 7.5 due to significant uncertainties related to large-scale structure. Typically, the PBHs with initial masses, denoted as $M_{\text{BH},i}$, less than a few solar masses face challenges in achieving efficient growth due to their low accretion rates. However, for PBHs with higher initial masses, the accretion process can be significantly more effective. In fact, some PBHs that originated in the very early Universe have the potential to grow to a size approaching $\sim 10^7 M_\odot$ (Kohri et al. 2022).

In the local Universe, a well-established trend reveals a shared growth pattern between SMBHs and galaxies, a relationship extensively discussed in the review by Greene et al. (2020). This co-evolution scenario is

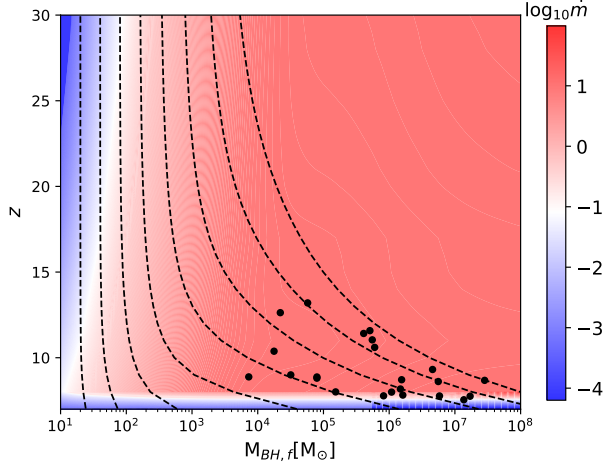


Figure 1. The accretion rate parameter \dot{m} , with mechanism feedback, as a function of the final mass of PBH $M_{\text{BH},f}$ and redshift z . The black points in the figure represent galaxy candidates identified from JWST observations, with a relation of $M_\star - M_{\text{BH}}$. The figure also shows trajectories of individual PBHs with $20M_\odot$, $40M_\odot$, $80M_\odot$, $160M_\odot$, $320M_\odot$, $640M_\odot$, $1280M_\odot$ and $2560M_\odot$ in the (M, z) plane, represented by black dotted lines.

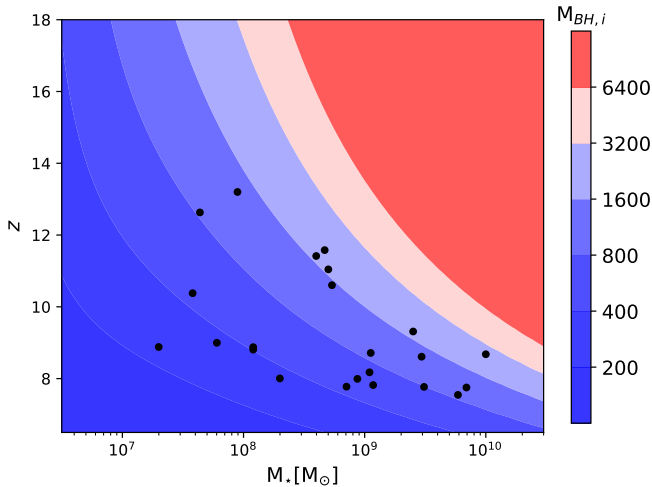


Figure 2. Initial PBH mass ($M_{\text{BH},i}$, represented by the colorbar) as a function of the galaxy mass M_\star and the redshift z . The candidates observed by JWST are represented by the black points, which has listed in Table 1.

believed to be influenced by feedback processes originating from active galactic nuclei (AGNs) and the initial mass density of SMBHs and galaxies. An empirical relationship between the mass of the SMBH, denoted as M_{BH} , and the galaxy mass M_\star is described by $\log M_{\text{BH}} = \alpha + \beta \log(M_\star/M_0) + \epsilon \log(1+z)$, where $M_0 = 3 \times 10^{10} M_\odot$ serves as a reference value. However, due to the absence of high-redshift measurements,

our understanding relies on theoretical extrapolation based on the values reported by [Greene et al. \(2020\)](#), which are $\alpha = 7.89 \pm 0.09$, $\beta = 1.33 \pm 0.12$ and $\epsilon = 0.2$. In Figure 2 we provide a visual representation of the initial mass, denoted as $M_{\text{BH},i}$, required to account for the current JWST observations of the high redshift massive galaxies, particularly within the context of the PBH accretion scenario using data obtained from the JWST.

3. JWST OBSERVATIONS AND PBH MASS DISTRIBUTION

The James Webb Space Telescope (JWST), launched on December 25, 2021, is the most powerful space telescope currently in operation, equipped with four instruments: Mid-Infrared Instrument (MIRI), Near-Infrared Spectrograph (NIRSpec), Near-Infrared Camera (NIRCam) and Fine Guidance Sensor/Near Infrared Imager and Slitless Spectrograph (FGS-NIRISS). During its Early Release Observations (EROs), the JWST observed the massive strong lensing cluster SMACSJ0723. Spectra obtained from this observation revealed both Ly α and Balmer breaks in the galaxies, offering valuable insights into their masses and redshifts through Spectral Energy Distribution (SED) fitting. Furthermore, the Cosmic Evolution Early Release Science (CEERS) program employed NIRCam to capture multi-band images in a deep field, covering an area of approximately 40 arcmin². These data have been widely utilized in numerous studies to identify candidates for massive high-redshift galaxies using the SED fitting method ([Labbe et al. 2022](#); [Atek et al. 2023](#); [Yan et al. 2023](#)).

However, it is essential to acknowledge that uncertainties persist in the photometric redshift estimation. Therefore, in this analysis, we focus on high-redshift JWST galaxy candidates with spectroscopically determined redshifts, which are more reliable ([Arrabal Haro et al. 2023](#); [Boyett et al. 2023](#); [Bunker et al. 2023](#); [Curtis-Lake et al. 2023](#); [Fujimoto et al. 2023](#); [Heintz et al. 2023](#); [Jung et al. 2023](#)). The galaxies included in Table 1 represent the most prominent candidates identified to date.

Furthermore, the Bondi accretion affects the mass distribution of PBHs with redshift. The fraction of PBHs with mass in the interval $(M, M + dM)$ at redshift z is what we refer to as the mass function $\psi(M, z)$. The evolution of an initial $\psi(M, z_i)$ at formation redshift z_i is governed by

$$\psi(M_f(M, z), z) dM_f = \psi(M, z_i) dM. \quad (2)$$

where $M_f(M, z)$ is the final mass of a PBH that accretes mass M at redshift z . In the literature, there are theoretical realizations for primordial power spectra that could generate a significantly enhanced power at small

Source ID	R.A. (deg)	Decl. (deg)	z_{spec}	$\log(M_*/M_\odot)$	Reference
CEERS-61419	214.897232	52.843854	$8.998^{+0.001}_{-0.001}$	$7.78^{+0.30}_{-0.30}$	Fu23
CEERS-61381	214.901252	52.846997	$8.881^{+0.001}_{-0.001}$	$7.30^{+0.30}_{-0.30}$	Fu23
CEERS-7078	215.011708	52.988303	$8.876^{+0.002}_{-0.002}$	$8.08^{+0.24}_{-0.30}$	Fu23
CEERS-4702	214.994404	52.989378	$8.807^{+0.003}_{-0.003}$	$8.08^{+0.22}_{-0.30}$	Fu23
CEERS-4774	215.005185	52.996577	$8.005^{+0.001}_{-0.001}$	$8.30^{+0.27}_{-0.22}$	Fu23
CEERS-4777	215.005365	52.996697	$7.993^{+0.001}_{-0.001}$	$8.94^{+0.24}_{-0.31}$	Fu23
CEERS-23084	214.830685	52.887771	$7.769^{+0.003}_{-0.003}$	$9.49^{+0.22}_{-0.24}$	Fu23
CEERS-43725	214.967532	52.932953	$8.715^{+0.001}_{-0.001}$	$9.05^{+0.03}_{-0.02}$	He23
CEERS-81061	215.035392	52.890667	$8.679^{+0.001}_{-0.001}$	$10.0^{+0.01}_{-0.01}$	He23
EGS-11855	215.218762	53.069862	$8.610^{+0.001}_{-0.001}$	$9.47^{+0.04}_{-0.06}$	He23
EGS-34697	215.089714	52.966183	$8.175^{+0.001}_{-0.001}$	$9.04^{+0.10}_{-0.11}$	He23
CEERS-59920	214.882994	52.840416	$7.820^{+0.001}_{-0.001}$	$9.07^{+0.01}_{-0.01}$	He23
EGS-8901	215.188413	53.033647	$7.776^{+0.001}_{-0.001}$	$8.85^{+0.07}_{-0.06}$	He23
EGS-33634	215.150862	52.989562	$7.752^{+0.001}_{-0.001}$	$9.84^{+0.44}_{-0.66}$	J23
EGS-36986	214.999053	52.941977	$7.546^{+0.001}_{-0.001}$	$9.77^{+0.51}_{-0.69}$	J23
CEERS-16943	214.943152	52.942442	$11.416^{+0.005}_{-0.005}$	$8.6^{+0.3}_{-0.3}$	AH23
CEERS-11384	214.906640	52.945504	$11.043^{+0.003}_{-0.003}$	$8.7^{+0.1}_{-0.1}$	AH23
GS-z10-0	53.15884	-27.77349	$10.38^{+0.07}_{-0.06}$	$7.58^{+0.19}_{-0.20}$	La23
GS-z11-0	53.16476	-27.77463	$11.58^{+0.05}_{-0.05}$	$8.67^{+0.08}_{-0.13}$	La23
GS-z12-0	53.16634	-27.82156	$12.63^{+0.24}_{-0.08}$	$7.64^{+0.66}_{-0.39}$	La23
GS-z13-0	53.14988	-27.77650	$13.20^{+0.04}_{-0.07}$	$7.95^{+0.19}_{-0.29}$	La23
GN-z11	189.10608333	62.2420556	$10.603^{+0.001}_{-0.001}$	$8.73^{+0.06}_{-0.06}$	Bu23
Gz9p3	3.617193	-30.4255352	$9.3127^{+0.0002}_{-0.0002}$	$9.40^{+0.11}_{-0.10}$	Bo23

Table 1. (1) Source ID corresponds to galaxies. (2) Right Ascension (R.A.) in J2000 coordinates, (3) Declination (Decl.) in J2000 coordinates; (4) Spectroscopic redshift values obtained from measurements of emission lines. (5) Mass of galaxies. (6) Literatures reporting these sources. [Fu23](#) (Fujimoto et al. 2023), [He23](#) (Heintz et al. 2023), [J23](#) (Jung et al. 2023), [AH23](#) (Arrabal Haro et al. 2023), [La23](#) (Curtis-Lake et al. 2023), [Bu23](#) (Bunker et al. 2023), and [Bo23](#) (Boyett et al. 2023).

scales allowing for an increase in the abundance of massive PBHs (Cai et al. 2023), such as non-attractor inflation (Kinney 2005; Martin et al. 2013; Garcia-Bellido & Ruiz Morales 2017) and non-perturbative resonance effects (Cai et al. 2018, 2019; Zhou et al. 2020; Cai et al. 2021). To distinguish various forms of theoretically predicted PBH mass functions, we consider the following typical PBH mass functions that arise in PBH formation models (Carr et al. 2021; Carr & Kuhnel 2020),

$$\psi_M = \begin{cases} \frac{1}{\sqrt{2\pi}\sigma M} \exp\left(-\frac{\log^2(M/M_c)}{2\sigma^2}\right) & \text{Lognormal,} \\ \sum_{n=1} A_n \delta(M - M_{cn}) & \text{Multipeak,} \\ \frac{1}{2} \frac{M_c^{1/2}}{M^{3/2}} \Theta(M - M_c) & \text{Powerlaw,} \\ \frac{1}{\sqrt{2\pi}\sigma} \exp\left(-\frac{(M-M_c)^2}{2\sigma^2}\right) & \text{Gaussian,} \\ \frac{3.2}{M} \left(\frac{M}{M_c}\right)^{3.85} \exp\left(-\left(\frac{M}{M_c}\right)^{2.85}\right) & \text{Critical.} \end{cases} \quad (3)$$

where $\Theta(M - M_c)$ is the step function, and the M_c , M_{cn} and σ are parameters in these distributions. For the Multipeak model, we use two normalized Gaussian distributions with same width in our analysis, as the evolution of $\delta(M - M_{cn})$.

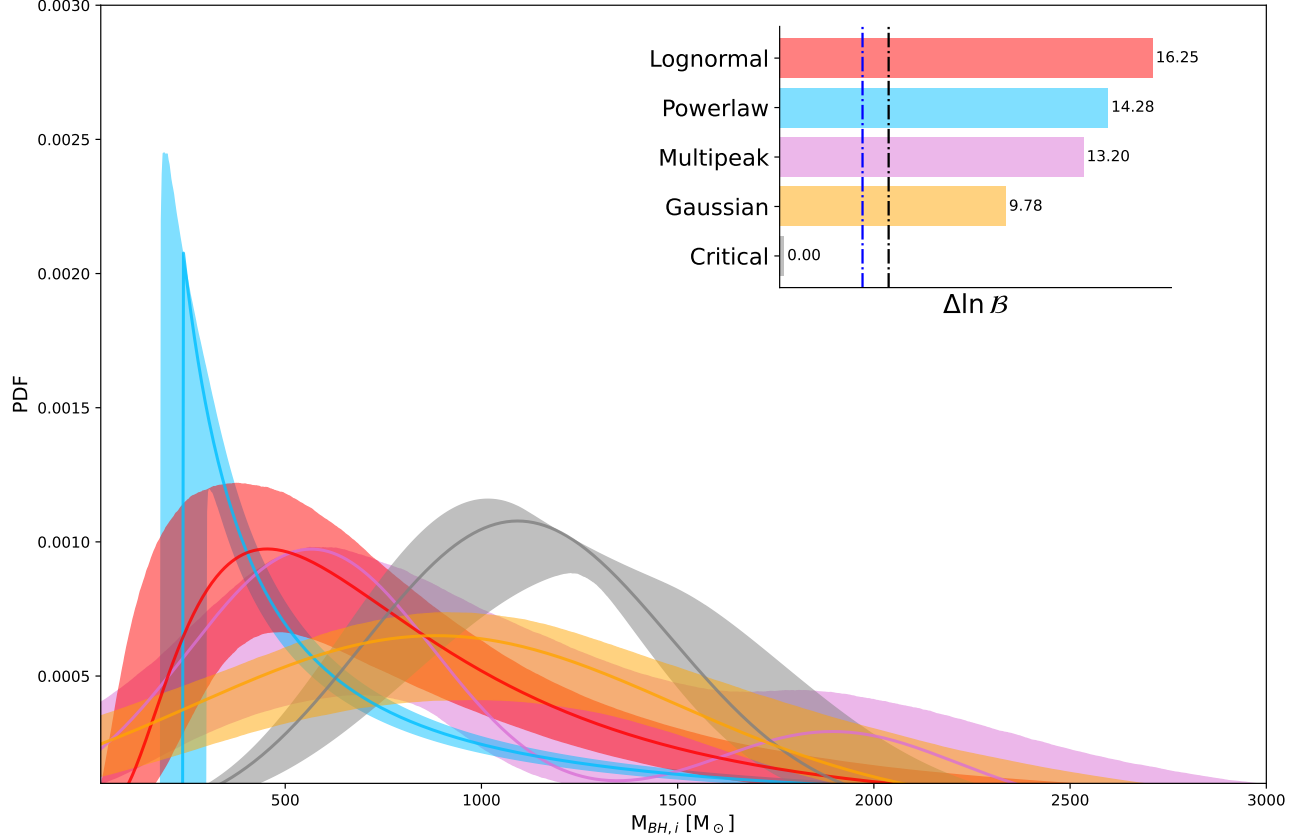


Figure 3. The posterior population distribution of the PBH models within a 90% credible interval. The distribution for Lognormal (red), Multipeak (orchid), Powerlaw (deepskyblue), Gaussian (orange) and Critical (grey) models are shown, with each line plotted using its optimal parameters. The Bayes factors for each model are displayed in the upper right corner, where the vertical dot-dashed lines indicate very strong evidence (blue) and decisive Bayesian evidence (black).

Models	x_e	M_c	σ	M_{c2}	f_{M_c}	N_{dof}	$\Delta \ln \mathcal{B}$	ΔAIC
Lognormal	$0.54^{+0.32}_{-0.36}$	$748.39^{+130.50}_{-111.08}$	$0.74^{+0.14}_{-0.11}$	-	-	2	16.25	0.00
Powerlaw	$0.60^{+0.28}_{-0.36}$	$242.65^{+34.43}_{-34.83}$	-	-	-	1	14.28	8.36
Multipeak	$0.45^{+0.37}_{-0.31}$	$675.16^{+167.36}_{-152.24}$	$457.38^{+173.04}_{-116.23}$	$1956.69^{+505.87}_{-420.64}$	$0.77^{+0.13}_{-0.16}$	4	13.20	8.22
Gaussian	$0.42^{+0.37}_{-0.29}$	$947.99^{+155.29}_{-150.46}$	$692.58^{+141.08}_{-105.48}$	-	-	2	9.78	10.68
Critical	$0.18^{+0.27}_{-0.13}$	$1142.07^{+94.12}_{-80.16}$	-	-	-	1	0.00	31.26

Table 2. Summary of the results for various initial mass functions of PBH. The first column lists the names of the models, followed by the 68% credible intervals of their parameters. The last two columns list the Bayes factor $\Delta \ln \mathcal{B}$ and the Akaike information criterion ΔAIC .

We use the masses of high-redshift galaxies recently observed by JWST to constrain the hyper-parameters λ of each initial PBH mass function through hierarchical Bayesian inference (Thrane & Talbot 2019). For a series of N independent observations, the posterior distribution for λ is given by

$$p(\lambda | d) = \pi(\lambda) \prod_i^N \int \mathcal{L}(d_i | \theta_i) p_{\text{pop}}(\theta_i | \lambda) d\theta_i, \quad (4)$$

where $\mathcal{L}(d_i | \theta_i)$ denote the likelihood function of the JWST data given a galaxy's properties θ_i (the mass and the redshift). The distribution of θ_i as predicted by the PBH population models is denoted by $p_{\text{pop}}(\theta_i | \lambda)$, which satisfies $p_{\text{pop}}(\theta_i | \lambda) = p(m)p(z)$, where $p(m)$ is the mass distribution of galaxies calculated from the initial PBH mass functions in Equation (3), and the galaxies are assumed to be distributed uniformly in the co-moving frame of the Universe. We assign Uniform priors $\pi(\lambda)$ for all of the hyper-parameters in this work. To approximate the reported result for the mass and

redshift of each galaxy (as shown by a central value plus/minus the uncertainties in Table 1), we use a two-dimensional skew normal distribution $\mathcal{N}(\theta_i)$, and assume that $\mathcal{L}(d_i | \theta_i) \propto \mathcal{N}(\theta_i)$. Then the above equation can be calculated via Monte Carlo integration with sample points drawn from the skew normal distributions.

To quantitatively evaluate various PBH models and the statistical significance of our results, we calculate the Bayes factor between model \mathcal{M}_1 and model \mathcal{M}_2 , namely $\mathcal{B}_{\mathcal{M}_2}^{\mathcal{M}_1} \equiv Z_{\mathcal{M}_1}/Z_{\mathcal{M}_2}$, where $Z_{\mathcal{M}} \equiv \int d\lambda p(\lambda | \mathbf{d})$. According to Jeffreys' scale criterion, a Bayes factor greater than $(10, 10^{1.5}, 10^2)$ (or $\ln Z$ larger than $[2.30, 3.45, 4.60]$) would suggest strong, very strong, or decisive Bayesian evidence in favor of model \mathcal{M}_1 relative to model \mathcal{M}_2 , given the available data. Additionally, we calculate the Akaike information criterion (AIC) (Akaike 1974), defining as $\text{AIC} \equiv 2N_{\text{dof}} - 2\ln(\mathcal{L}(d_i | \theta_i))$, to compare models with different numbers of parameters. A difference of ΔAIC of 2 or more indicates strong evidence against the model with the higher AIC value.

Our summarized results, presented in Table 2, reveal a preference for the Lognormal, Powerlaw, and Multi-peak models over the Gaussian models, with a Bayesian evidence $\ln(\mathcal{B})$ exceeding 3.42. Furthermore, the Lognormal model outperforms the Powerlaw and Multi-peak models, and the Powerlaw and Multi-peak models exhibit comparable quality as indicated by their slight differences in BIC and AIC values. Notably, the Critical model displays the highest AIC value and the lowest BIC value, thus being strongly disfavored. Figure 3 displays the constraints on the five different PBH initial mass functions and the Bayes factors of each model compared to the Critical model. The colored shaded zones represent the 90% credible regions for the inferred population distribution. For all models, the majority of the PBH masses lie $\sim 1000M_{\odot}$. According to Jeffreys' scale criterion, the logarithmic Bayes factors for the Lognormal model, the Powerlaw model, the Multi-peak model, and the Gaussian model are 16.25, 14.28, 13.20, and 9.78, respectively, indicating they are decisively preferred by the data compared to the Critical model. Most notably, the Lognormal mass function stands out from the five models, with the lowest AIC value of 8.36 compared to the second preferred model. Consequently, we conclude that JWST observations provide informative insights into distinguishing the initial PBH mass function, with current data offering relatively stringent constraints on its shape. Moreover, the above analysis also highlights the importance of statistical analysis in making conclu-

sions about the PBHs population and their implications for early cosmology.

4. SUMMARY

The accretion of baryonic matter onto PBHs is believed to have played an important role in the early Universe, giving rise to the formation of seed black holes at the centers of early galaxies. This study demonstrates that PBHs with initial masses of $\sim 1000 M_{\odot}$ exhibit rapid growth through accretion, reaching masses in the range of $\sim 10^6 - 10^8 M_{\odot}$ by $z \gtrsim 7$, which could potentially account for the massive high-redshift galaxies observed by JWST. Future observations with JWST during the cosmic re-ionization era are expected to reveal these rapidly growing PBHs, as their accretion can yield energetic radiation across a broad spectrum of wavelengths. Consequently, this radiation could initiate the formation of a group of luminous active galactic nuclei, which might manifest as high-redshift compact objects, akin to recent observations made by JWST (Furtak et al. 2022). In our efforts to constrain the formation models of PBHs, we have employed a hierarchical Bayesian inference framework, leading to a strong preference for the Lognormal Model with a characteristic mass of $M_c \sim 750M_{\odot}$ over other scenarios.

It is noteworthy that the initial mass distribution of the PBHs uncovered in our study significantly differs from that expected in the pair-instability supernova scenario (Abel et al. 2002; Heger et al. 2003), which is characterized by an abrupt cutoff in the mass function at $\sim 40M_{\odot}$ (Li et al. 2023). However, it's essential to exercise caution, as the current high-redshift galaxy sample remains relatively limited, and future data may influence the current model constraints. Nevertheless, our current results have demonstrated the promising prospect of distinguishing between different PBH distribution models with future observation.

ACKNOWLEDGEMENTS

We are grateful to Lei Feng, Qiang Yuan and Lei Zu for helpful discussion. This work is supported in part by the National Key R&D Program of China (2021YFC2203100), by the NSFC (11921003, 11961131007, 11653002, 12003029, 12261131497), by China Postdoctoral Science Foundation under grant No. 2023TQ0355, by CAS Young Interdisciplinary Innovation Team (JCTD-2022-20), by 111 Project for "Observational and Theoretical Research on Dark Matter and Dark Energy" (B23042), by the Fundamental Research Funds for Central Universities, by the CSC Innovation Talent Funds, by the CAS project for young scientists in basic research (YSBR-006), and by the USTC Research Funds of the Double First-Class Initiative.

REFERENCES

- Abel, T., Bryan, G. L., & Norman, M. L. 2002, *Science*, 295, 93
- Akaike, H. 1974, *IEEE Transactions on Automatic Control*, 19, 716
- Ali-Haïmoud, Y., & Kamionkowski, M. 2017, *Phys. Rev. D*, 95, 043534
- Arrabal Haro, P., Dickinson, M., Finkelstein, S. L., et al. 2023, *Nature*, 622, 707
- Atek, H., Shuntov, M., Furtak, L. J., et al. 2023, *MNRAS*, 519, 1201
- Bertschinger, E. 1985, *ApJS*, 58, 39
- Biagetti, M., Franciolini, G., & Riotto, A. 2023, *ApJ*, 944, 113
- Bird, S., Cholis, I., Muñoz, J. B., et al. 2016, *Phys. Rev. Lett.*, 116, 201301
- Bosch-Ramon, V. 2022, *Astron. Astrophys.*, 660, A5
- Bosch-Ramon, V., & Bellomo, N. 2020, *Astron. Astrophys.*, 638, A132
- Boyett, K., Trenti, M., Leethochawalit, N., et al. 2023, *arXiv e-prints*, arXiv:2303.00306
- Bunker, A. J., Saxena, A., Cameron, A. J., et al. 2023, *A&A*, 677, A88
- Cai, Y.-F., Chen, C., Tong, X., Wang, D.-G., & Yan, S.-F. 2019, *Phys. Rev. D*, 100, 043518
- Cai, Y.-F., Jiang, J., Sasaki, M., Vardanyan, V., & Zhou, Z. 2021, *Phys. Rev. Lett.*, 127, 251301
- Cai, Y.-F., Tong, X., Wang, D.-G., & Yan, S.-F. 2018, *Phys. Rev. Lett.*, 121, 081306
- Cai, Y.-F., Tang, C., Mo, G., et al. 2023, *arXiv e-prints*, arXiv:2301.09403
- Cai, Y.-F., Tang, C., Mo, G., et al. 2023, *arXiv:2301.09403*
- Carr, B., Kohri, K., Sendouda, Y., & Yokoyama, J. 2021, *Rept. Prog. Phys.*, 84, 116902
- Carr, B., & Kuhnelt, F. 2020, *Ann. Rev. Nucl. Part. Sci.*, 70, 355
- Curtis-Lake, E., Carniani, S., Cameron, A., et al. 2023, *Nature Astronomy*, 7, 622
- De Luca, V., Franciolini, G., Pani, P., & Riotto, A. 2020a, *Phys. Rev. D*, 102, 043505
- . 2020b, *JCAP*, 04, 052
- Escrivà, A., Kuhnelt, F., & Tada, Y. 2022, *arXiv:2211.05767*
- Fujimoto, S., et al. 2023, *Astrophys. J. Lett.*, 949, L25
- Furtak, L. J., Zitrin, A., Plat, A., et al. 2022, *arXiv e-prints*, arXiv:2212.10531
- Garcia-Bellido, J., & Ruiz Morales, E. 2017, *Phys. Dark Univ.*, 18, 47
- Gardner, J. P., et al. 2006, *Space Sci. Rev.*, 123, 485
- Green, A. M., & Kavanagh, B. J. 2021, *J. Phys. G*, 48, 043001
- Greene, J. E., Strader, J., & Ho, L. C. 2020, *Ann. Rev. Astron. Astrophys.*, 58, 257
- Hawking, S. 1971, *MNRAS*, 152, 75
- Heger, A., Fryer, C. L., Woosley, S. E., Langer, N., & Hartmann, D. H. 2003, *Astrophys. J.*, 591, 288
- Heintz, K. E., Brammer, G. B., Giménez-Arteaga, C., et al. 2023, *Nature Astronomy*, arXiv:2212.02890
- Hütsi, G., Raidal, M., Urrutia, J., Vaskonen, V., & Veermäe, H. 2023, *PhRvD*, 107, 043502
- Inayoshi, K., Visbal, E., & Haiman, Z. 2020, *Ann. Rev. Astron. Astrophys.*, 58, 27
- Jung, I., Finkelstein, S. L., Arrabal Haro, P., et al. 2023, *arXiv e-prints*, arXiv:2304.05385
- Kinney, W. H. 2005, *Phys. Rev. D*, 72, 023515
- Kohri, K., Sekiguchi, T., & Wang, S. 2022, *PhRvD*, 106, 043539
- Labbe, I., van Dokkum, P., Nelson, E., et al. 2022, *Nature*, arXiv:2207.12446
- Li, Y.-J., Wang, Y.-Z., Tang, S.-P., & Fan, Y.-Z. 2023, *arXiv e-prints*, arXiv:2303.02973
- Liu, B., & Bromm, V. 2022, *Astrophys. J. Lett.*, 937, L30
- Lovell, C. C., Harrison, I., Harikane, Y., Tacchella, S., & Wilkins, S. M. 2023, *MNRAS*, 518, 2511
- Mack, K. J., Ostriker, J. P., & Ricotti, M. 2007, *Astrophys. J.*, 665, 1277
- Martin, J., Motohashi, H., & Suyama, T. 2013, *Phys. Rev. D*, 87, 023514
- Montero-Camacho, P., Fang, X., Vasquez, G., Silva, M., & Hirata, C. M. 2019, *JCAP*, 08, 031
- Perivolaropoulos, L., & Skara, F. 2022, *New Astron. Rev.*, 95, 101659
- Piga, L., Lucca, M., Bellomo, N., et al. 2022, *JCAP*, 12, 016
- Ricotti, M. 2007, *Astrophys. J.*, 662, 53
- Ricotti, M., Ostriker, J. P., & Mack, K. J. 2008, *Astrophys. J.*, 680, 829
- Sasaki, M., Suyama, T., Tanaka, T., & Yokoyama, S. 2016, *Phys. Rev. Lett.*, 117, 061101, [Erratum: *Phys.Rev.Lett.* 121, 059901 (2018)]
- Serpico, P. D., Poulin, V., Inman, D., & Kohri, K. 2020, *Phys. Rev. Res.*, 2, 023204
- Thrane, E., & Talbot, C. 2019, *Publ. Astron. Soc. Austral.*, 36, e010, [Erratum: *Publ.Astron.Soc.Austral.* 37, e036 (2020)]
- Trinca, A., Schneider, R., Maiolino, R., et al. 2023, *MNRAS*, 519, 4753
- Volonteri, M., Habouzit, M., & Colpi, M. 2021, *Nature Rev. Phys.*, 3, 732
- Yan, H., Ma, Z., Ling, C., Cheng, C., & Huang, J.-S. 2023, *ApJL*, 942, L9

Zel'dovich, Y. B., & Novikov, I. D. 1966, *Astron. Z.*, 43, 758

Zhou, Z., Jiang, J., Cai, Y.-F., Sasaki, M., & Pi, S. 2020, *Phys. Rev. D*, 102, 103527

APPENDIX: THE POSTERIOR DISTRIBUTION OF PBH POPULATION

The posteriors of the hyper-parameters describing the initial mass distributions of PBHs (Lognormal/Gaussian/Powerlaw/Critical/Multipeak), as introduced in the main text, are displayed in Figure 4, respectively.

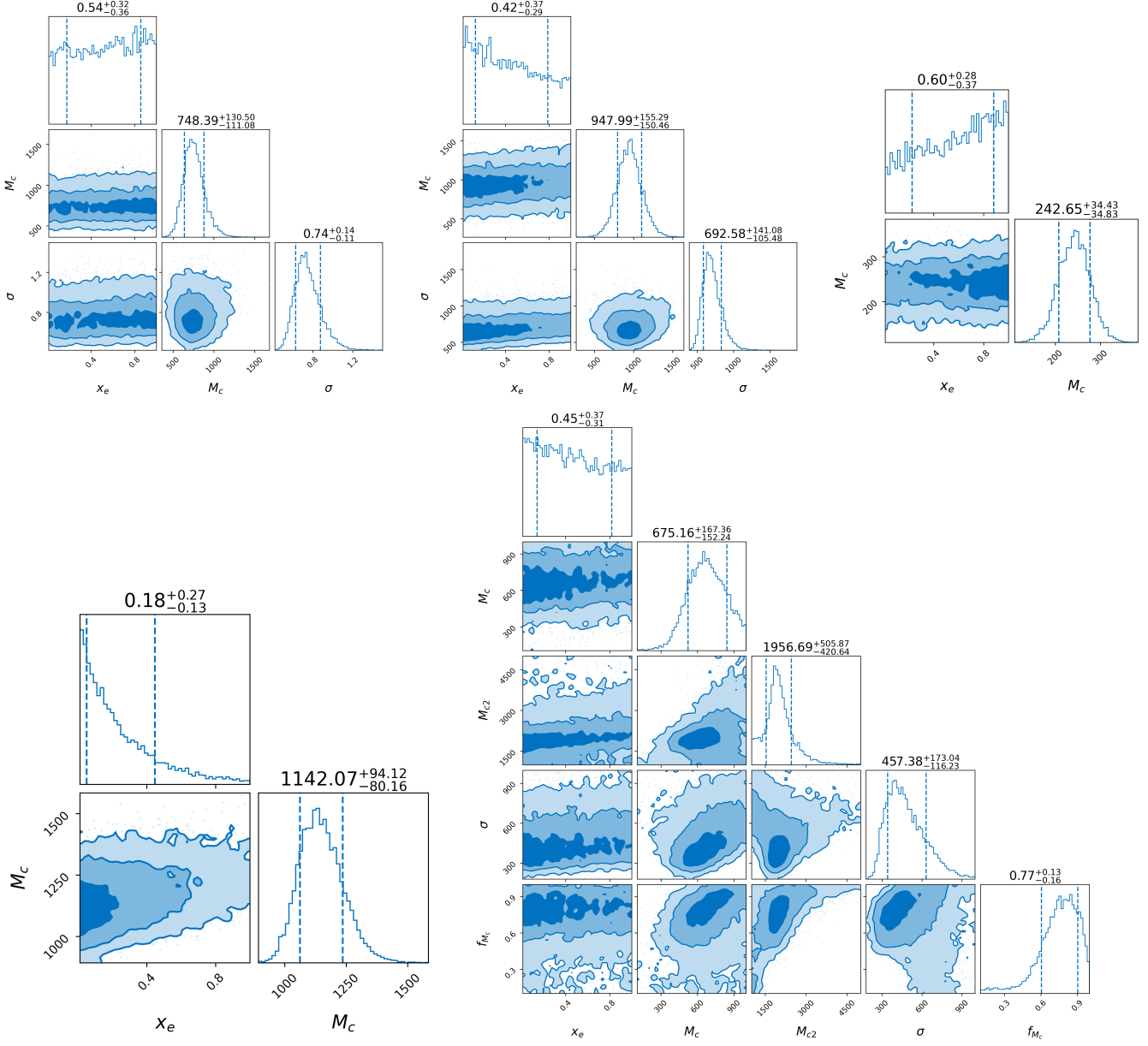


Figure 4. The posterior distributions of individual parameters for five different population models. The upper panels from left to right panels show the results for the Lognormal, Gaussian and Powerlaw models, respectively. While the lower left and right panels refer to the Critical and Multipeak models. All models include the ionization fraction of the cosmic gas x_e , and we use the parameters listed in Table 2 with Uniform priors. The 68% confidence intervals for each parameter are reported above each column, corresponding to the models shown in the inset.